

## Development of an optical flow through detector for bubbles, crystals and particles in oils

Peter R. Birkin<sup>a\*</sup>, Jack J. Youngs<sup>a</sup>, Tadd T. Truscott<sup>b</sup> and Silvana Martini<sup>c</sup>

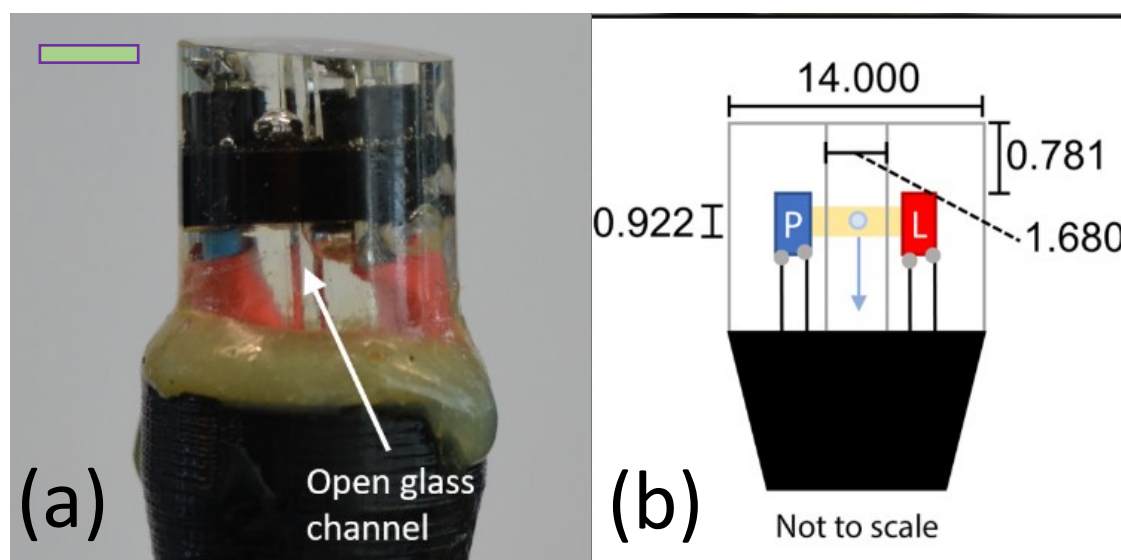
<sup>a</sup> Department of Chemistry, University of Southampton, Southampton, UK, SO17 1BJ, UK.

<sup>b</sup> Department of Mechanical and Aerospace Engineering, Utah State University, Logan, UT, 84322-4130, USA.

<sup>c</sup> Department of Nutrition, Dietetics, and Food Sciences, Utah State University, Logan, UT, 84322-8700, USA.

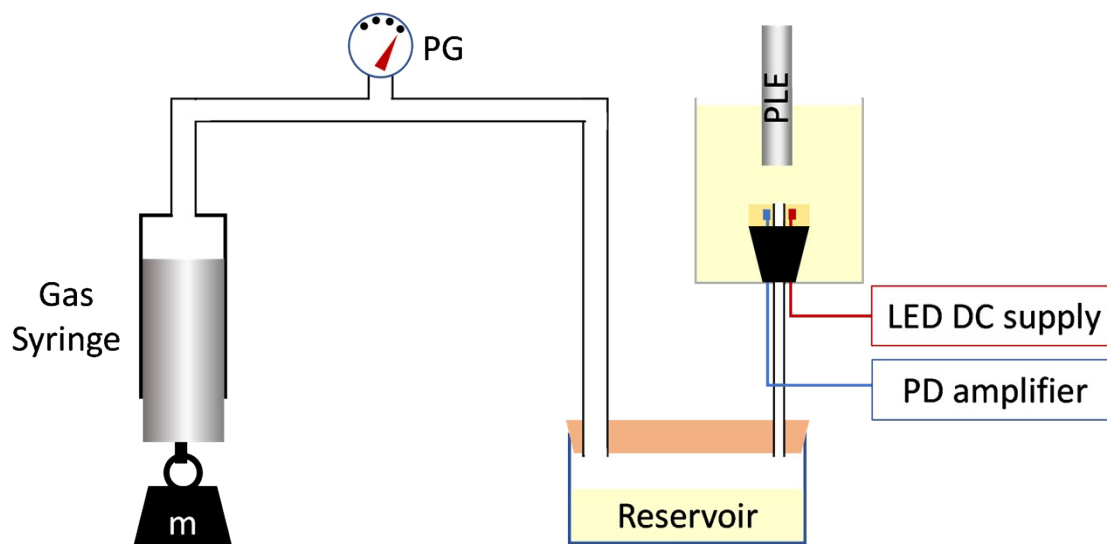
\* Corresponding author, prb2@soton.ac.uk.

Figure S1 shows a schematic representation and an image of the optical transmission sensor (OTS). The device was constructed using a 3D printed scaffold and epofix resin (Struers) to secure the components in place.



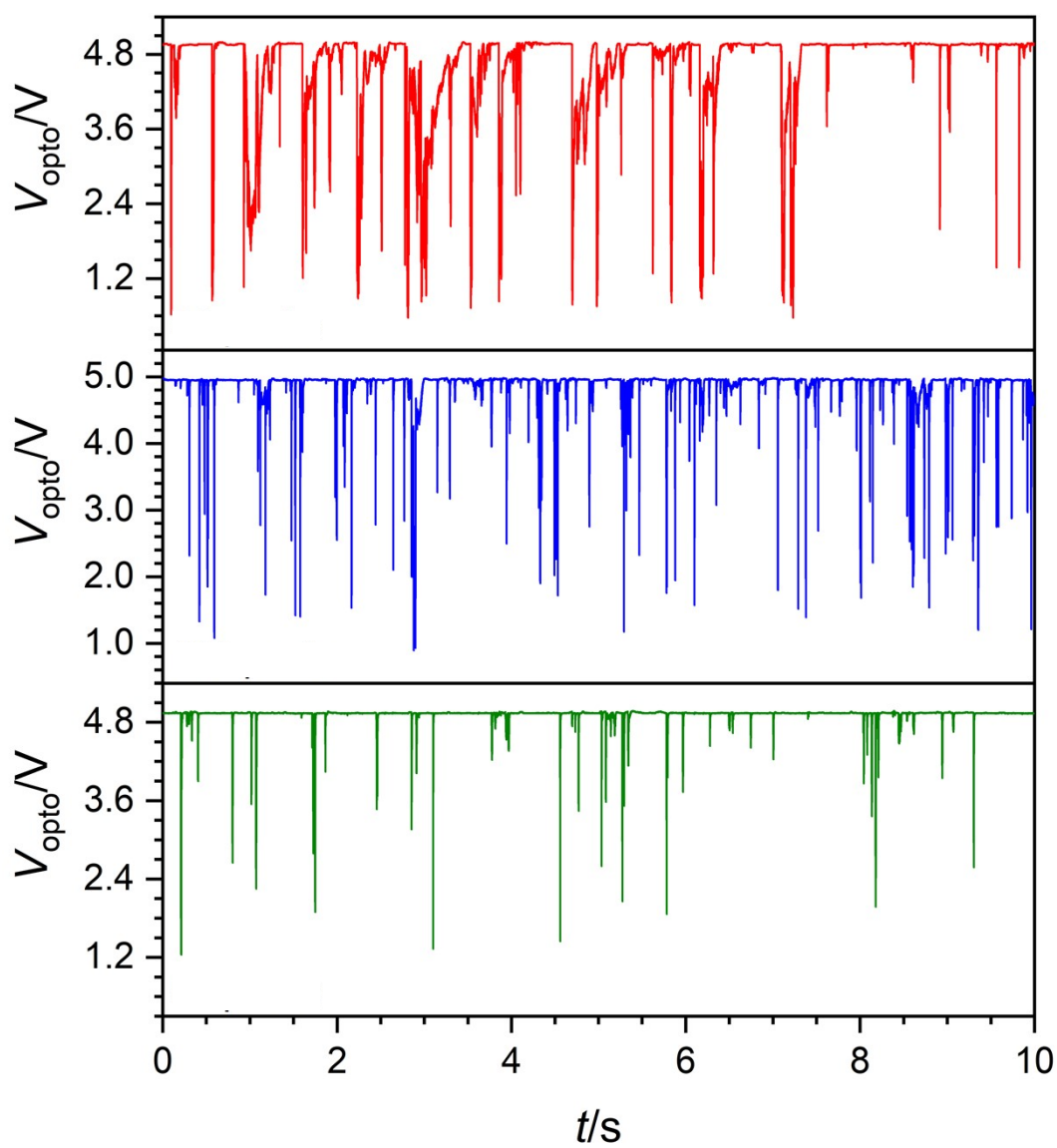
**Figure S1.** Image depicting the side view (a) of the OTS device. The scale bar represent 5 mm. Schematic (b) shows the approximate dimensions (in mm) of the LED (L) and photodiode (P) components within the opto-counter device with respect to the central open glass capillary channel. The bubble detection region (shown in yellow) is highlighted as a gas bubble or crystal is drawn through the device (see blue arrow). Note, not to scale.

Figure S2 shows the pressure rig used to draw the oil through the OTS device. In this case a small reservoir was used to capture oil that had been drawn through the device and prevent it from entering the piping to the pressure gauge.



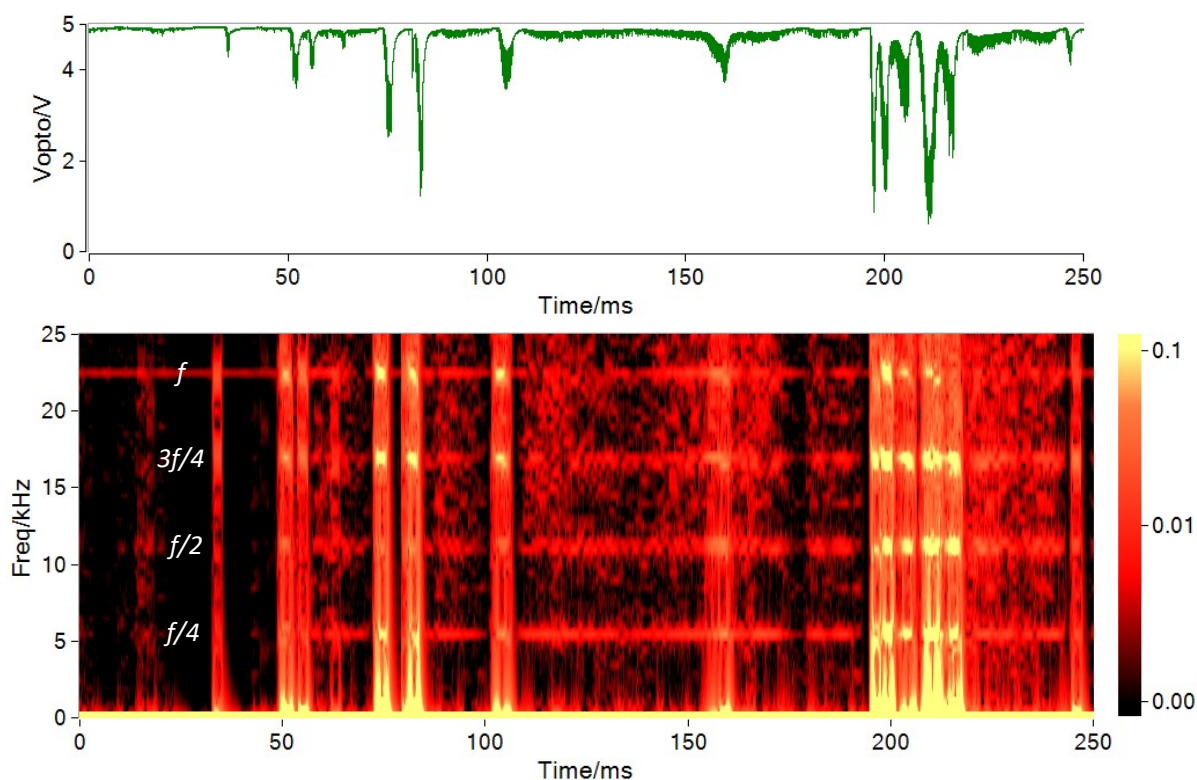
**Figure S2.** Schematic representation of the pressure system and the cell. Included are the gas syringe and a mass (m) to pull a constant pressure on the oil through the OTS device. A reservoir is included which captures oil passed through the device. A pressure gauge (PG) was used to monitor the pressure within the system.

Figure S3 shows the effect of horizontal motion of the OTS device with respect to the HIU source. In this case, as the OTS channel is moved laterally away from the cluster formed at the HIU tip, the event frequency falls. This suggests that the bubble density is highest close to the cluster as expected.



**Figure S3.** Plots showing the OTS signal recorded with the device in aerobic liquid soybean oil (SBO) over 10 sec period. Each plot depicts the translocation of gas bubbles generated by HIU with a PLE tip driven at  $32 W_{RMS}$  ( $f \sim 22.6$  kHz). The PLE was secured 2 mm above the plane of the OTS support with a horizontal displacement of 0 mm (—), 2 mm (—) and 5 mm (—) from the channel opening of the device. A pressure differential of -113 mbar was applied across the opto-counter channel and the sample temperature was  $24.1$  °C.

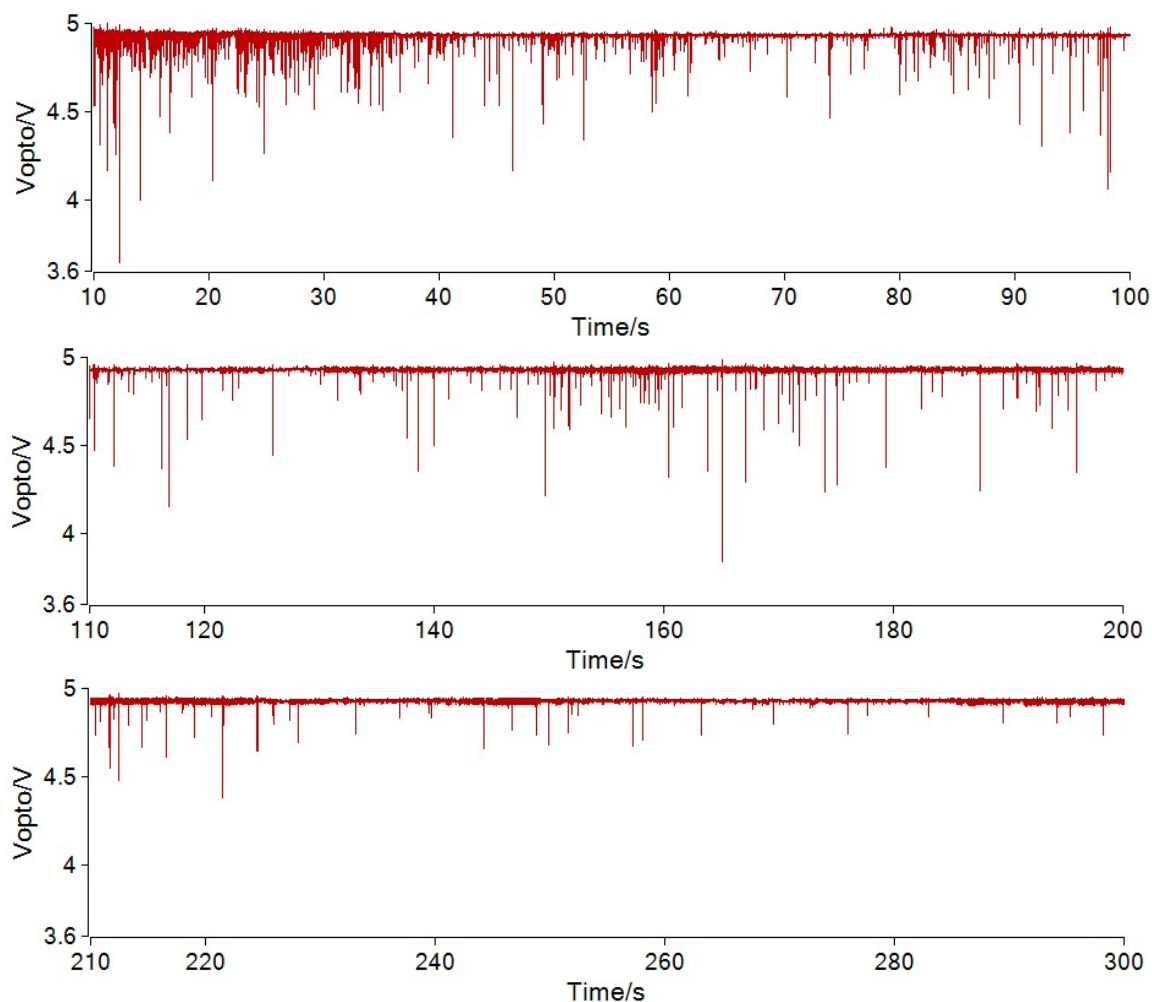
Figure S4 shows a section of OTS signal and the corresponding frequency analysis. In this case the HIU drive conditions produced an  $f/4$  cluster as indicated by the frequency components detected in the OTS signal.



**Figure S4.** Plots showing the OTS signal as a function of time (—). The sample consisted of SBO. An ultrasonic power of  $18 W_{rms}$  was employed. The data was captured at  $5 \times 10^5$  Hz with a pressure differential applied across the OTS channel for gas bubble detection of -114 mbar. The SBO was at  $26$  °C. The lower plot shows the subharmonic components. In this case the data shows the presence of a response indicative of an  $f/4$  cluster. The individual components are marked for reference.

The OTS was used to monitor the bubble population in a soybean oil (SBO) sample. Figure S5 shows the OTS signal as a function of time after a 10 s burst of HIU had been applied to the cell. The data shows that the bubble population is highest directly after the HIU had been terminated (10-110 s) and then gradually decayed away with fewer and fewer large events seen. This indicates that as the time increased after the HIU exposure the bubble population in the oil fell with the larger bubbles lost first, presumably through natural buoyancy effects. However, even after 300 s there are small events detected by the OTS sensor indicating that the bubble population persists for a significant period of

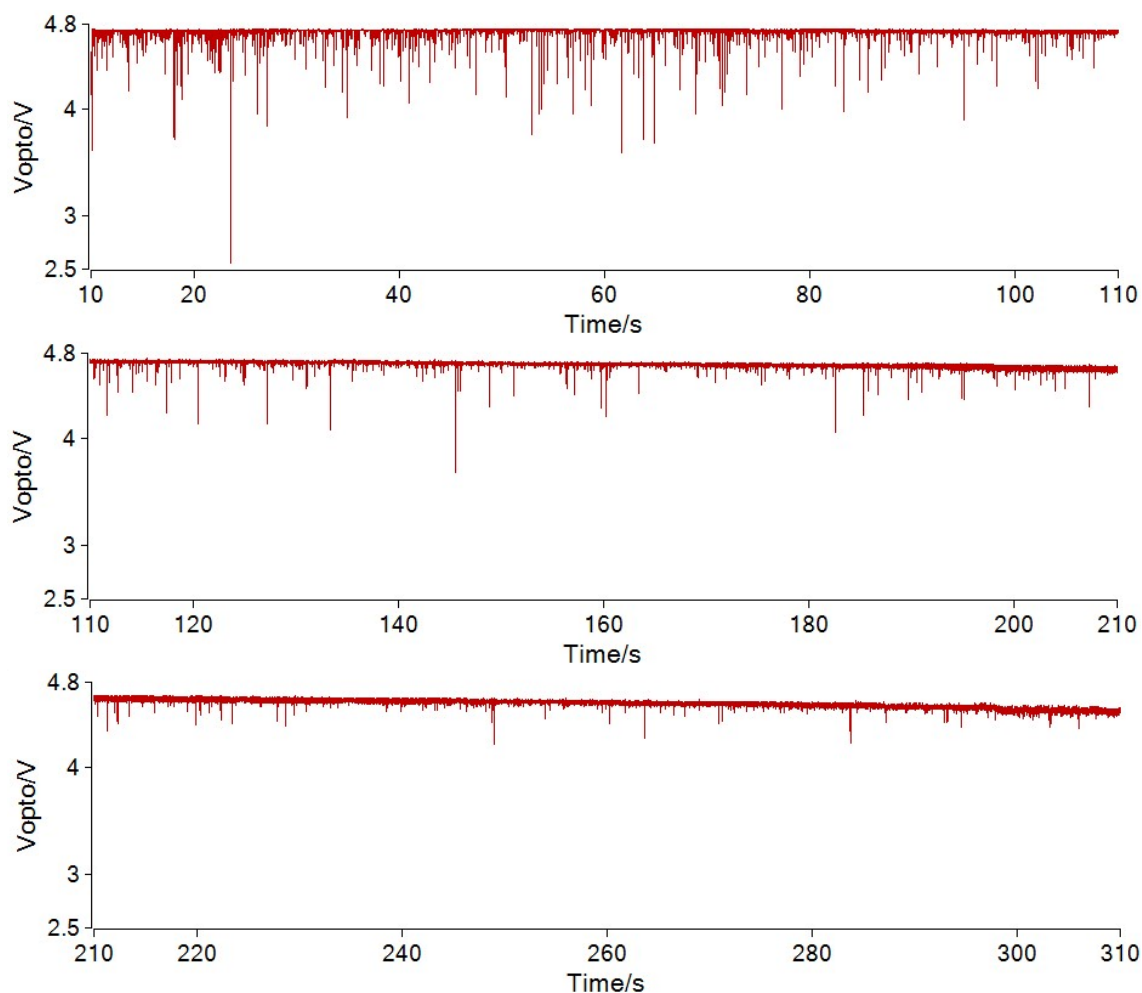
time after the HIU exposure. Lastly, the baseline remains constant throughout this experiment. This suggests that the bulk opacity of the media remains unchanged as expected for SBO.



**Figure S5.** Plot showing the OTS signal as a function of time recorded in SBO (—). The plots depict the translocation of ultrasonically generated gas bubbles for a total 300 sec period after PLE operation was terminated. HIU was applied within the sample with a PLE tip driven at 75 W ( $f = 20$  kHz) between Time = 0 - 10 s. The opto-counter was positioned centrally at the base of the cell. The PLE was secured 2 mm above the opto-counter surface with a horizontal displacement of 2 mm from the channel opening. The pressure differential applied across the opto-counter channel was -113 mbar and the sample temperature was 26.1°C.

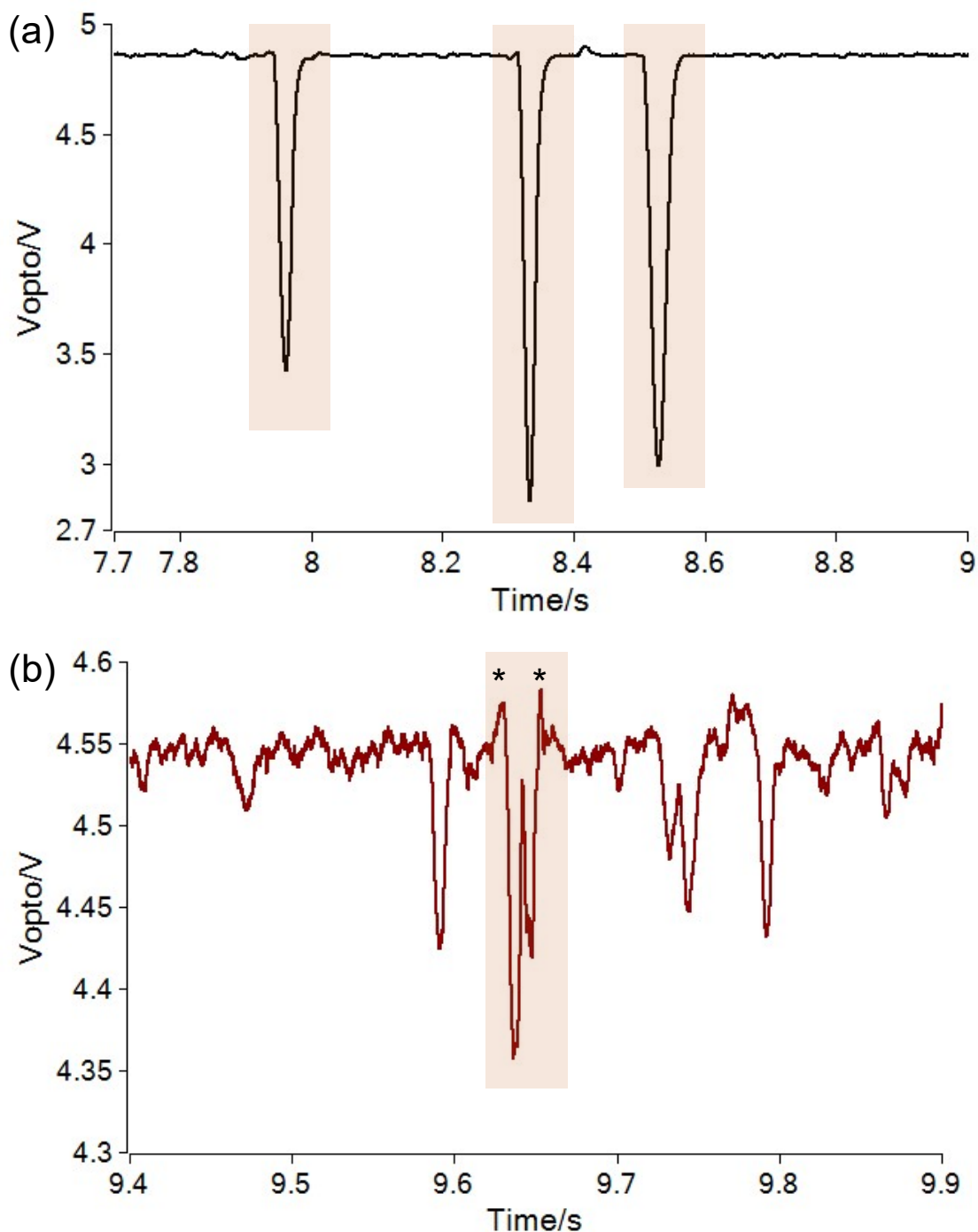
Figure S6 shows the OTS signal as a function of time for a sample of all-purpose shortening (APS) below the crystallisation temperature. The data also shows that the bubble population is highest directly after the HIU had been terminated (10-110 s) and then gradually decayed away with fewer and fewer large events seen. This indicates that as the time increased after the HIU exposure the bubble population in the oil fell with the larger bubbles lost first, presumably through natural buoyancy effects. However, even after 300 s there are small events detected by the OTS sensor indicating that the bubble population persists for a significant period after the HIU exposure. Lastly, the baseline in

this case does not remain constant throughout this experiment. This suggests that the bulk opacity of the media falls the APS starts to crystallise. This is in contrast to SBO as expected under these conditions.



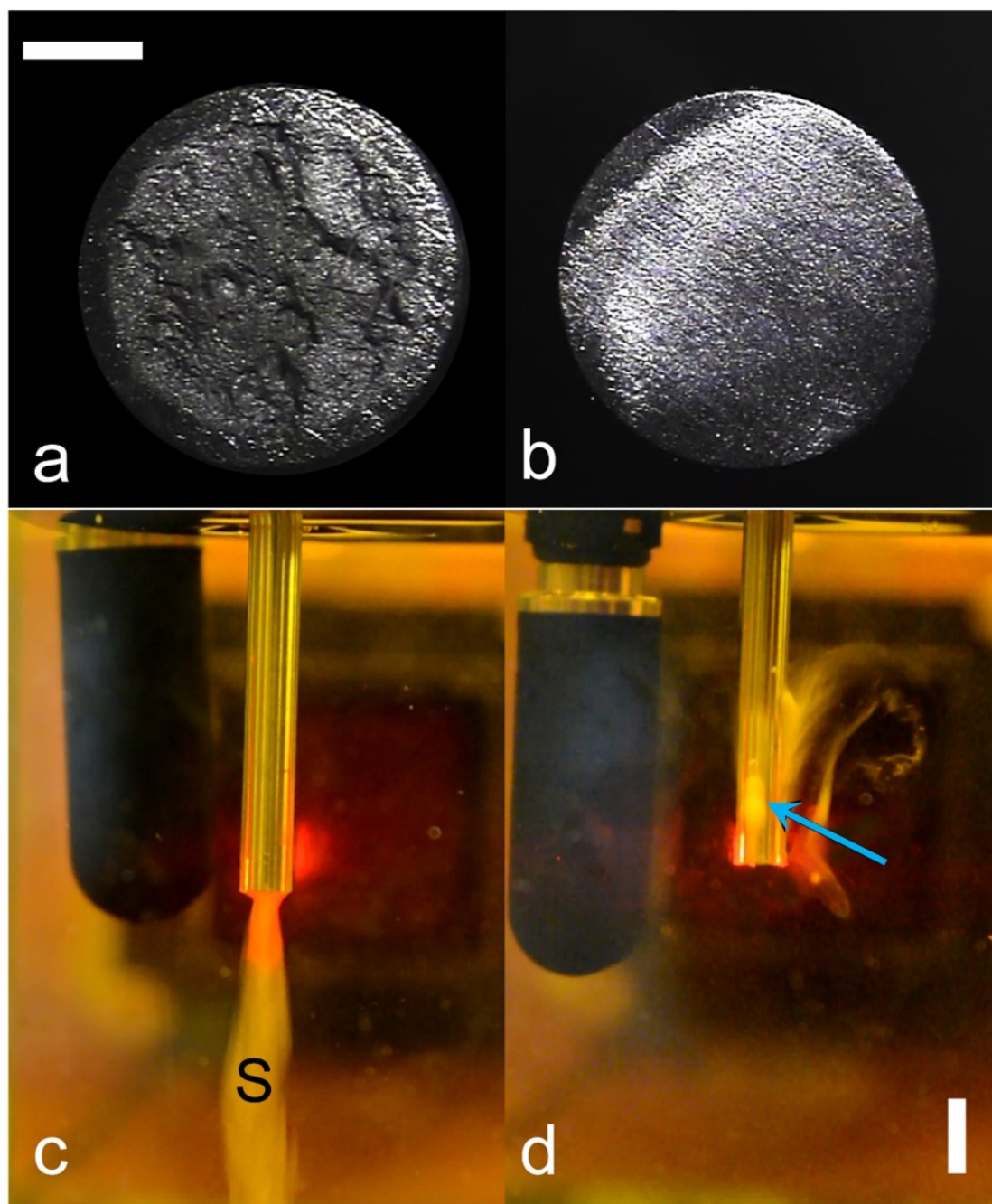
**Figure S6.** Plot showing the OTS signal as a function of time recorded in APS (—). The plots depict the translocation of ultrasonically generated gas bubbles for a total 300 sec period after PLE operation was terminated. HIU was applied within the sample with a PLE tip driven at 75 W ( $f = 20$  kHz) between  $t = 0 - 10$  s. The opto-counter was positioned centrally at the base of the cell. The PLE was secured 2 mm above the opto-counter surface with a horizontal displacement of 2 mm from the channel opening. The pressure differential applied across the opto-counter channel was -113 mbar and the sample temperature was 30.0°C.

Figure S7a shows the response of the sensor to glassy carbon spheres. Note, in this case the positive transients were not detected. In contrast, figure S7b shows the response of the sensor to a relatively large spherulite. In this case, positive deviations are seen at the beginning and end of the translocation of the spherulite through the OTS device. Although the data acquisition and processing conditions are slightly different, these results suggest that these positive transients are associated with the fat spherulite. However, this seems associated with the large signals detected indicating that this may also be an effect associated with clusters of spherulites within the detection zone of the OTS. Note, these transients are relatively small compared to the complete signal detected. Clearly, further investigation of this effect is needed to ascertain the nature of this effect.



**Figure S7a.** Plot showing the OTS response as a series of glassy carbon calibration spheres suspended in oil were passed through the channel. The data was recorded at 10 kHz sample rate. **Figure S7b** shows the OTS signal as a function of time for a large spherulite, or cluster of spherulites passing through the channel in an APS sample. The data was sampled at 200 kHz and a 25-point moving average applied in this case. The highlight shows the larger transients selected. The ‘\*’ highlights the positive signals seen for the APS sample at the beginning and end of the highlighted translocation event.

To generate the stable clusters used in these investigations, an eroded tip is advantageous. Figure S8 (a) and (b) show images of the eroded tip surface and polished surface respectively. The bubble cloud for each tip is shown in figure S8 (c) and (d) respectively.



**Figure S8.** Images recorded to illustrate the surface effects of the PLE tip during operation in liquid soybean oil. (a) Eroded tip, (b) polished tip, (c) side profile of cavitation cluster and streamer regimes located on the eroded PLE tip (a). The presence of the stable bubble streamer, (S), is highlighted in (c). Image (d) instead depicts bubble activity on the polished tip (b) and the blue arrow indicates the existence of an unstable bubble cluster to the side of the PLE. The scale bar represents 1 mm for images (a) and (b) and 5 mm in images (c) and (d). HIU was applied at  $\sim 32 W_{\text{RMS}}$  for both surface conditions and the temperature was  $\sim 24$  °C.

To calibrate the OTS device a variety of particles were deployed. This included a sample of glassy carbon particles. These were first sized using an optical microscopy technique with appropriate image analysts. The resultant distribution was also compared to the description provided by the manufacturer. Figure S9 shows a representative image and the associated determined distribution.

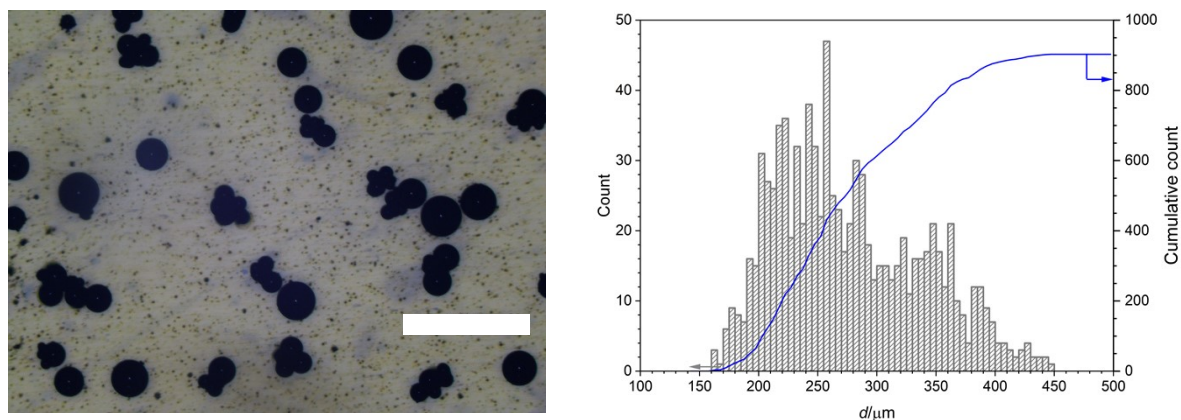


**Figure S9** Left: Optical microscopy image of glassy carbon spheres (manufacturer quoted 200-400  $\mu\text{m}$  diameter) used for calibration of the OTS device affixed to a glass slide with a strip of adhesive polyimide tape and recorded at 3x magnification. The scale bar represents 1000  $\mu\text{m}$ . Right: histogram of particle diameters calculated from microscopy images of glassy carbon spheres. The plot has horizontal bin widths of 5  $\mu\text{m}$  and the blue line (—) shows the cumulative count of the distribution. Microscopy images were analysed using ImageJ software.

Figure 10 shows the calibration data for the OTS and the glassy carbon particles.

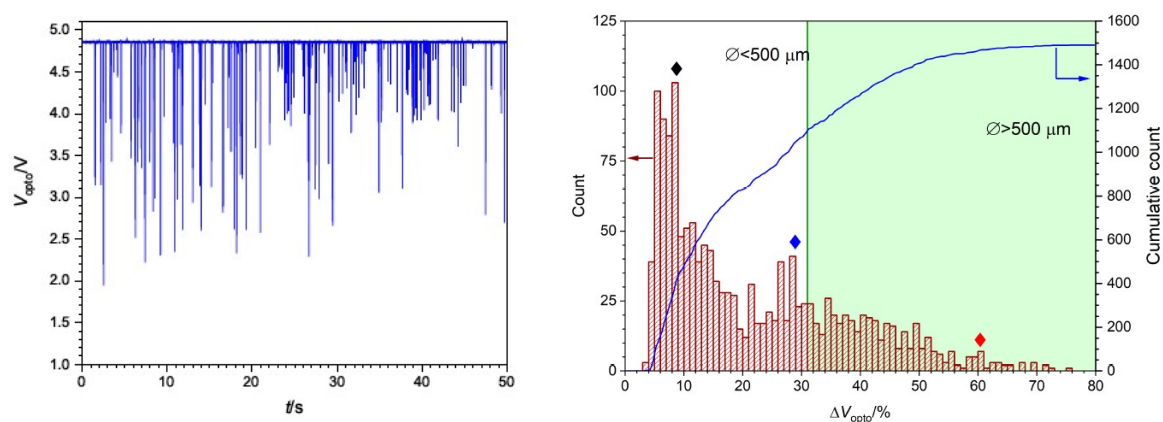


**Figure S10.** Left: Plot showing the response of the opto-counter device ( $V_{\text{opto}}$ ) as a function of time as glassy carbon spheres ( $\varnothing = 200\text{-}400 \mu\text{m}$ ) were drawn through the OTS at a negative pressure of approximately -113 mbar. Spheres were suspended within a soybean oil sample and agitated in an ultrasound bath prior to experiment. Right: Histogram of the change in the OTS signal (as  $\Delta V_{\text{opto}}/\%$ ) recorded from the translocation of calibration particles ( $\varnothing = 200\text{-}400 \mu\text{m}$ ) through the device. The red bars show the number of events for each bin width of 2% and the blue line (—) shows the cumulative count. Changes in the device response greater or equal to that observed for 500 mm diameter spheres (30.2%) are highlighted by green shading and are confirmed by inspection of events in this region (see figure S11). The symbols correspond to the single particle range matching those shown in figure S9.

To complete the calibration, the histograms from both the optical microscopy and the response of the OTS device ( $V_{\text{opto}}$ ) were overlaid, discounting the events which have been shown to correspond

to double/multiple events (see figure S11). The estimated response of the OTS device at 200  $\mu\text{m}$  and 400  $\mu\text{m}$  sizes could then be determined from this smaller distribution.

Figure S11 shows events associated with the OTS response. These are used to identify conglomerate translocations through the OTS, which occur predominately in the shaded region of figure S10.

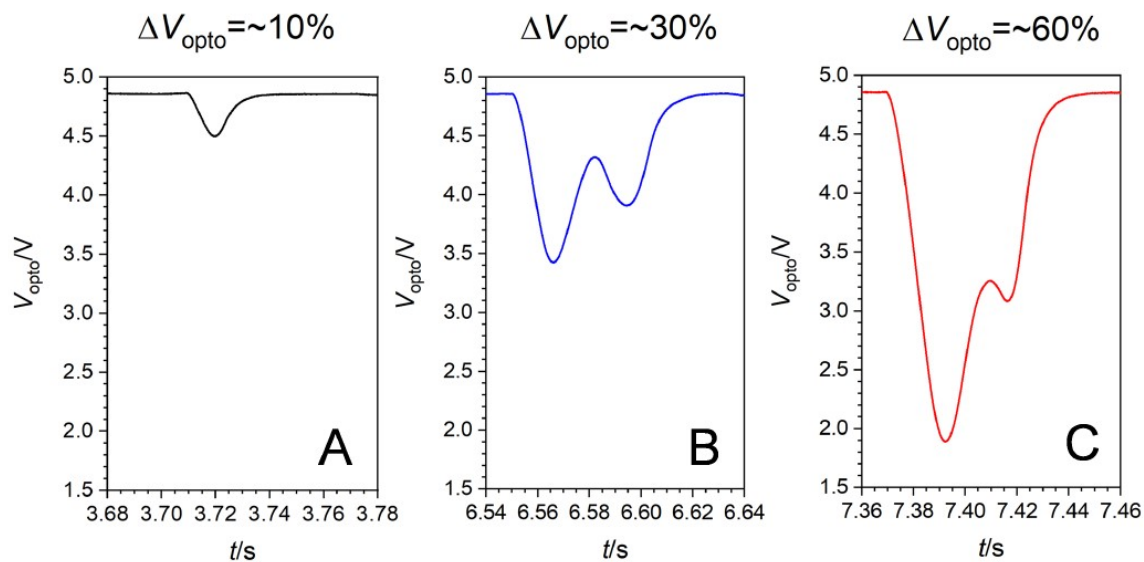


**Figure S11.** Plots depicting the shape of the translocation events recorded by the OTS device using the polydispersed calibration sphere suspension ( $\varnothing = 200 - 400 \mu\text{m}$ ). The three selected events were representative of the three regions identified within Figure S10 where  $\Delta V_{\text{opto}}$  was  $\sim 10\%$  (—)(A),  $\sim 30\%$  (—)(B); or  $\sim 60\%$  (—)(C).